Chemical
Science

EDGE ARTICLE

View Article Online
View Journal | View Issue

Open Access Article. Published on 27 July 2023. Downloaded on 7/14/2025 8:56:35 PM.
This article is licensed under a Creative Commons Attribution-NonCommercial 3.0 Unported Licence.

Check for updates

Cite this: *Chem. Sci.*, 2023, **14**, 8914

All publication charges for this article have been paid for by the Royal Society of Chemistry

Received 25th April 2023
Accepted 25th July 2023

DOI: 10.1039/d3sc02109b

rsc.li/chemical-science

Surface polarization-induced emission and stability enhancement of $CsPbX_3$ nanocrystals†

Keqiang Chen,[abcd] Zixin Gu,[a] Zhiqing Wang,[b] Mengyu Guan,[a] Xiu Tan,[a] Wanqing Xu,[a] Xinyu Ji,[a] Weiqi Lu,[a] Yueli Liu *[b] and Guogang Li *[ac]

Recently, the polarization effect has been receiving tremendous attention, as it can result in improved stability and charge transfer efficiency of metal-halide perovskites (MHPs). However, realizing the polarization effect on $CsPbX_3$ NCs still remains a challenge. Here, metal ions with small radii (such as Mg^{2+}, Li^+, Ni^{2+}, *etc.*) are introduced on the surface of $CsPbX_3$ NCs, which facilitate the arising of electric dipole and surface polarization. The surface polarization effect promotes redistribution of the surface electron density, leading to reinforced surface ligand bonding, reduced surface defects, near unity photoluminescence quantum yields (PLQYs), and enhanced stability. Moreover, further introduction of hydroiodic acid results in the *in situ* formation of *tert*-butyl iodide (TBI), which facilitates the successful synthesis of pure iodine-based $CsPbI_3$ NCs with high PLQY (95.3%) and stability under ambient conditions. The results of this work provide sufficient evidence to exhibit the crucial role of the surface polarization effect, which promotes the synthesis of high-quality MHPs and their applications in the fields of optoelectronic devices.

Introduction

All-inorganic $CsPbX_3$ (X = Cl, Br, I) perovskite nanocrystals (NCs) represent a flourishing area of research over the past decade, owing to their impressive optoelectronic properties, including strong light-absorption coefficients, photoluminescence (PL) with a narrow full width at half-maximum (FWHM) and high quantum yields, exceptional defect tolerance, and long carrier diffusion lengths. All these properties make them ideal candidates for a wide range of applications such as solar cells, light-emitting diodes (LEDs), lasers, and photodetectors.[1–8] However, the poor stability of $CsPbX_3$ NCs greatly limits their wide applications, which should be primarily ascribed to their ionic bonding nature induced highly dynamic surface ligands.[9–13] The loss of surface ligands would lead to the formation of halide vacancies, and eventually to the failure of the crystal structure with substantial degradation of photoluminescence quantum yields (PLQYs).[14–20] Therefore, much effort has been dedicated to passivate the surface of $CsPbX_3$ NCs by introducing various kinds of ligands with enhanced bonding energy, such as trioctylphosphine (TOP),[21] 2,2′-iminodibenzoic acid (IDA),[22] glutathione,[23] 4-bromo-butyric acid,[24] *etc.*[25–32]

Our previous report suggested that short-chain ligands (such as octanoic acid and octylamine) possess larger polarity in comparison to the commonly used oleylamine (OLA) and oleic acid (OA). The increased polarity leads to stronger adsorption energy, which can result in improved structural stability of $CsPbX_3$ NCs.[33] Moreover, it is well known that the polarity is closely related to dielectric properties, that is, a highly polarized material has a larger dielectric constant, which facilitates the charge transfer process.[34–37] Recently, Liu *et al.* suggested that an increase in the dielectric constant could result in a decrease in the electrostatic force between the defects and carriers, which reduced the defect-capture radius.[38] In addition, introducing dipolar molecules is known to be an effective way to enhance the stability of perovskite.[39–41] Li *et al.* employed a dipole layer between organic transport layers and inorganic perovskite, leading to reduced energetic mismatch and increased charge extraction.[41] Therefore, it is clear from previous studies that increasing the surface polarization of $CsPbX_3$ NCs potentially provides an alternative strategy to strengthen the surface ligand bonding and decrease the defect-capture radius. However, a dipolar-molecule-based dipole layer is most commonly used to achieve the polarization effect in bulk perovskites,[42] and this strategy is not suitable for $CsPbX_3$ NCs dispersed in non-polar solvent with a small size (~10 nm). It is reasonable to suppose that inducing distortion into the intrinsic surface

---

[a] *Faculty of Materials Science and Chemistry, China University of Geosciences, Wuhan, 430074, P. R. China. E-mail: ggli@cug.edu.cn*

[b] *State Key Laboratory of Advanced Technology for Materials Synthesis and Processing, State Key Laboratory of Silicate Materials for Architectures, School of Materials Science and Engineering, Wuhan University of Technology, Wuhan, 430070, P. R. China. E-mail: lylliuwhut@whut.edu.cn*

[c] *Zhejiang Institute, China University of Geosciences, Hangzhou, 311305, China*

[d] *Shenzhen Research Institute, China University of Geosciences, Shenzhen, 518052, China*

† Electronic supplementary information (ESI) available. See DOI: https://doi.org/10.1039/d3sc02109b

© 2023 The Author(s). Published by the Royal Society of Chemistry

Open Access Article. Published on 27 July 2023. Downloaded on 7/14/2025 8:56:35 PM.
This article is licensed under a Creative Commons Attribution-NonCommercial 3.0 Unported Licence.

structure of $CsPbX_3$ NCs might be a feasible way to realize the polarization effect.

In this contribution, we develop a co-solvent assisted reprecipitation (CSARP) strategy to synthesize $CsPbX_3$ NCs under ambient conditions. Various kinds of metal halides (such as MgX_2, $X = Cl, Br, I$) with relatively smaller ionic radii (compared with the Pb^{2+} ion) are employed as halide precursors; sufficient halide ions can passivate the surface halide vacancies. More importantly, the metal ions with small radii would distort the metal-halide octahedron (such as $[MgBr_6]^{4-}$, which prefers to emerge on the surface of $CsPbX_3$ NCs), resulting in the arising of surface polarization. As a result, $CsPbX_3$ NCs with reduced surface defect density and improved surface ligand bonding are achieved, leading to near unity photoluminescence quantum yields (PLQYs) and enhanced stability. This phenomenon is further verified by using metal ions with various ionic radii. Moreover, pure iodine-based $CsPbI_3$ NCs can be directly synthesized by the introduction of hydroiodic acid. Our results provide a facile solution for the preparation of $CsPbX_3$ NCs with optimized optoelectronic properties and enhanced stability.

Results and discussion

In the commonly used ligand-assisted reprecipitation (LARP) approach, DMF/DMSO are employed as "good solvents" to dissolve metal halide salts (such as CsBr or $PbBr_2$), and expectedly, these solvents would also lead to the failure of the as-formed perovskite structure.[43] Therefore, the strategy adopted in this study is to dissolve metallic and halide precursors separately, which can minimize the negative effect of solvents. Fig. S1† presents a schematic illustration of the synthetic process of $CsPbX_3$ NCs *via* our co-solvent assisted reprecipitation (CSARP) strategy. Briefly, Cs^+ and Pb^{2+} precursors dissolved in acetic acid are added to a mixture of *n*-hexane, *tert*-butanol alcohol (TBA), OLA, and OA to form a homogeneous solution. Successively, a halide precursor (such as MgX_2, $X = Cl$ and Br) dissolved in water (HI for MgI_2) is injected into the above solution, resulting in the formation of the desired $CsPbX_3$ NCs; detailed information can be found in Experimental section, Fig. S2, Tables S1 and S2.† Here, TBA is employed as a transitionary solvent to balance the huge discrepancy between hexane and water (or hydriodic acid). In the absence of TBA, the immiscibility of hexane and water leads to the failure of the formation of perovskite NCs, as the metal and halide precursors are dissolved in hexane and water (or hydriodic acid), respectively.

To start with, $MgBr_2$ is used as a halide precursor to synthesize $CsPbBr_3$ NCs. Fig. 1a shows typical optical images of the as-synthesized $CsPbBr_3$ NCs under room light and a UV lamp ($\lambda = 365$ nm), respectively. A strong green emission emerges under a UV lamp, which is quite an expected result. Interestingly, however, prominent PL emission is also observed even under room light, which clearly suggests the remarkable optical properties of the as-prepared $CsPbBr_3$ NCs. The UV-vis absorption spectrum of the as-synthesized $CsPbBr_3$ NCs shown in Fig. 1b exhibits a clear excitonic absorption peak and absorption centered at 2.480 eV. In addition, near-unity PLQY with the emission peak at 2.431 eV is shown. The small Stokes shift (49 meV) suggests a direct exciton recombination process. These results further confirm the near ideal optical properties

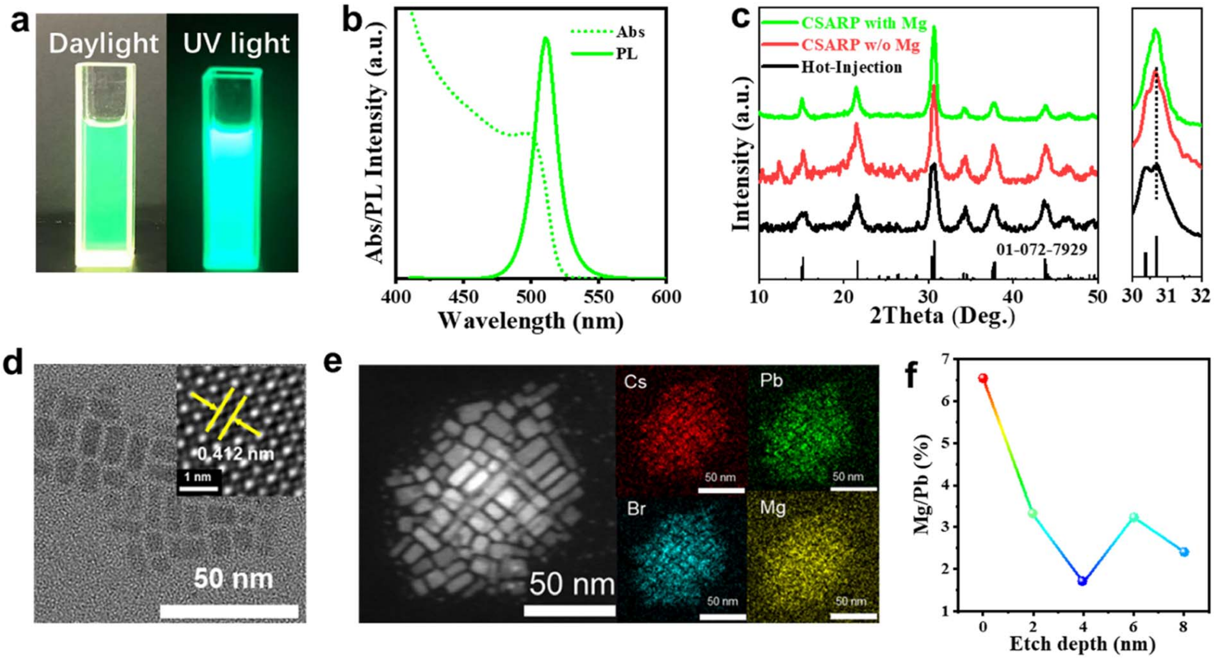

Fig. 1 (a) Photographs of CSARP-$CsPbBr_3$ NCs under room light (left) and a UV lamp (right, $\lambda = 365$ nm). (b) UV-vis and PL spectra of CSARP-$CsPbBr_3$ NCs. (c) X-ray diffraction pattern of CSARP-$CsPbBr_3$ NCs with/without Mg^{2+} ions and hot-injection-$CsPbBr_3$, the right inset shows the magnified XRD patterns for the 2θ region of 30–32°. (d) TEM image of the CSARP-$CsPbBr_3$ NCs (inset: HRTEM). (e) EDX mappings of the CSARP-$CsPbBr_3$ NCs. (f) The Mg/Pb ratio in CSARP-$CsPbBr_3$ NCs for various etching depths.

© 2023 The Author(s). Published by the Royal Society of Chemistry

Open Access Article. Published on 27 July 2023. Downloaded on 7/14/2025 8:56:35 PM.
This article is licensed under a Creative Commons Attribution-NonCommercial 3.0 Unported Licence.

of the as-synthesized $CsPbBr_3$ NCs. More discussions on the synthesis process can be found in ESI Note 1, Fig. S2, and Table S1.† X-ray diffraction (XRD) patterns and transmission electron microscope (TEM) images shown in Fig. 1c and d verify the pure phase and regular morphology of the as-synthesized $CsPbBr_3$ NCs (Fig. S3†).[44,45] Furthermore, the high-angle annular dark-field (HAADF) scanning TEM (STEM) image and the energy-dispersive X-ray spectroscopy (EDX) mappings shown in Fig. 1e reveal that a small amount of Mg^{2+} ions is uniformly dispersed in the NCs. Quantitative analysis of the EDX results further suggests that the atom ratio between Mg and Pb is about 5.2%. Compared with the XRD pattern of NCs synthesized through CSARP with/without Mg^{2+} ions and a hot-injection process, the diffraction peaks almost remain unchanged (Fig. 1c). Moreover, the NCs are further *in situ* etched by argon ion bombardment on the surface for various depths. It is clearly shown in Fig. 1f that the atom ratio of Mg/Pb is 6.6% at the very surface of NCs, which is also well in agreement with the EDX results. With the increase of etching depth, the atom ratio of Mg/Pb decreases rapidly (2–3%). Therefore, it can be inferred that Mg^{2+} ions should emerge on the surface of $CsPbBr_3$ NCs.[46]

Density functional theory (DFT) calculations are further taken into account to provide a comprehensive understanding on the role of Mg^{2+} ions in $CsPbBr_3$ NCs. It is known that the adsorption of protonated OLA (H^+-OLA) on the surface of $CsPbBr_3$ NCs is crucial for their stability and optoelectronic properties.[13] There is no net polarization on the surface of pure $CsPbBr_3$ NCs due to the fact that the Pb atom is almost at the exact center of the $[PbBr_6]^{4-}$ octahedron void, as shown in Fig. 2a. In contrast, when the Pb atoms on the surface layer are replaced by Mg atoms, their relatively smaller ionic radii remarkably increase the distortion of $[MgBr_6]^{4-}$ octahedra (Fig. 2b). The lattice distortion drives the Mg atoms off the octahedral center, leading to the misalignment of positive and negative charges on the surface of $CsPbBr_3$ NCs. As a result, the microscopic particles form an electric dipole and exhibit polarity. The surface polarization directly promotes the redistribution of the surface electron density, and the Br atom located right above the Mg atom (Fig. 2d, one Pb atom on the surface layer replaced by one Mg atom, marked as 1Mg) has higher electron density compared to that in pure $CsPbBr_3$ (Fig. 2c). This phenomenon is also observed for the completely substituted one (*i.e.*, all the Pb atoms on the surface layer are replaced by Mg atoms, marked as *n*Mg, Fig. 2e). The enhanced electron density facilitates the adsorption of the protonated OLA with increased adsorption energy (E_{ads}), which is found to be 5.457, 5.805, and 6.021 eV for pure $CsPbBr_3$, 1Mg-, and *n*Mg-$CsPbBr_3$, respectively (*trans*-OLA with negligible polarity is selected for the calculation to exclude the influence of capping ligands). Furthermore, this observation could be also verified by differential charge density (Fig. 2f and g), which exhibits increased net interfacial electron transfer and a reduced Br-OLA bond length as the Mg atoms are introduced. Therefore, it is reasonable to conclude that the excellent optical properties of the as-synthesized $CsPbBr_3$ NCs can be attributed to the reduced halide-vacancy density and enhanced surface ligand bonding.

In order to have a more comprehensive understanding of the relationship between the polarity and optical properties of perovskite NCs, we further carry out a series of calculations based on various kinds of alkaline-earth metal halides (Be, Mg, Ca, Sr, and Ba). As shown in Fig. 3, destructive lattice distortions of $[BeBr_6]^{4-}$ and $[BaBr_6]^{4-}$ octahedra can be clearly observed when Pb atoms in the $[PbBr_6]^{4-}$ octahedra are replaced by Be and Ba atoms, which should be ascribed to their unsuitable radii (either too small or too large). That is to say, Be^{2+} and Ba^{2+} are not suitable for the synthesis of perovskite NCs. In contrast, when $MgBr_2$, $CaBr_2$, and $SrBr_2$ are employed as precursors, all of $[MgBr_6]^{4-}$, $[CaBr_6]^{4-}$, and $[SrBr_6]^{4-}$ octahedra can be well maintained. Moreover, $[MgBr_6]^{4-}$ and $[SrBr_6]^{4-}$ octahedra exhibit the largest ($\Delta_D = 0.12$) and smallest ($\Delta_D = 0.06$) distortions, respectively. Therefore, we hypothesize that when alkaline-earth metal halides are used as precursors for the synthesis of perovskite NCs *via* the CSARP strategy, $MgBr_2$, $CaBr_2$, and $SrBr_2$ could result in luminescent phase NCs, and the $MgBr_2$-based one should possess the highest PLQY, while $BeBr_2$ and $BaBr_2$ would lead to non-luminescent phase NCs.

Whereafter, $CsPbBr_3$ NCs are synthesized using alkaline-earth metal halides as precursors *via* the CSARP process (as $BeBr_2$ is unavailable, there are no corresponding data). From Fig. 3f, one can clearly find that Mg^{2+}-based $CsPbBr_3$ NCs exhibits the champion PLQY (~100%), while the PLQYs of Ca^{2+}-(86%) and Sr^{2+}-(52%) based ones decrease in turn. Interestingly, the Ba^{2+}-based one leads to the emergence of non-luminescent phase NCs (PLQY = 0%). As the concentration of Br^- in these reactions is the same, therefore, the distinct discrepancy of the PLQY should be attributed to the arising of various kinds of cations. These outcomes are entirely consistent with the aforementioned theory calculations, which also provide substantial evidence for the previous supposition.

Likewise, the crucial relationships between the ionic radius, polarity, and optical properties are further verified by employing various kinds of metal halides (including LiBr, NaBr, RbBr, NH_4Br, $NiBr_2$, $ZnBr_2$, and $InBr_3$) as precursors for the synthesis of $CsPbBr_3$ NCs. The PLQYs of NCs based on these precursors are shown in Fig. 3f. A clear tendency, that is, the PLQY having a negative correlation with the cation radius, can be observed. Within a proper range of cation radii, the PLQY can be estimated through the following equation:

$$\text{PQLY}\% = 190.13 - 1.26r \qquad (1)$$

where *r* represents the cation radius. It is worth noting that the PLQY does not exhibit an obvious correlation with the oxidation states of cations, which further confirms the crucial role of the cation radius. In summary, we can conclude that the cation radius dominates the polarity of metal-halide octahedra; within an appropriate range, a smaller cation radius leads to a larger surface polarization. Moreover, perovskite NCs can possess enhanced PLQY and stability with increasing surface polarization.

For comparison, $CsPbBr_3$ NCs are also prepared *via* the widely used LARP strategy (denoted as LARP-$CsPbBr_3$ NCs). Optical property characterization studies shown in Fig. 4a and

© 2023 The Author(s). Published by the Royal Society of Chemistry

Open Access Article. Published on 27 July 2023. Downloaded on 7/14/2025 8:56:35 PM.
This article is licensed under a Creative Commons Attribution-NonCommercial 3.0 Unported Licence.

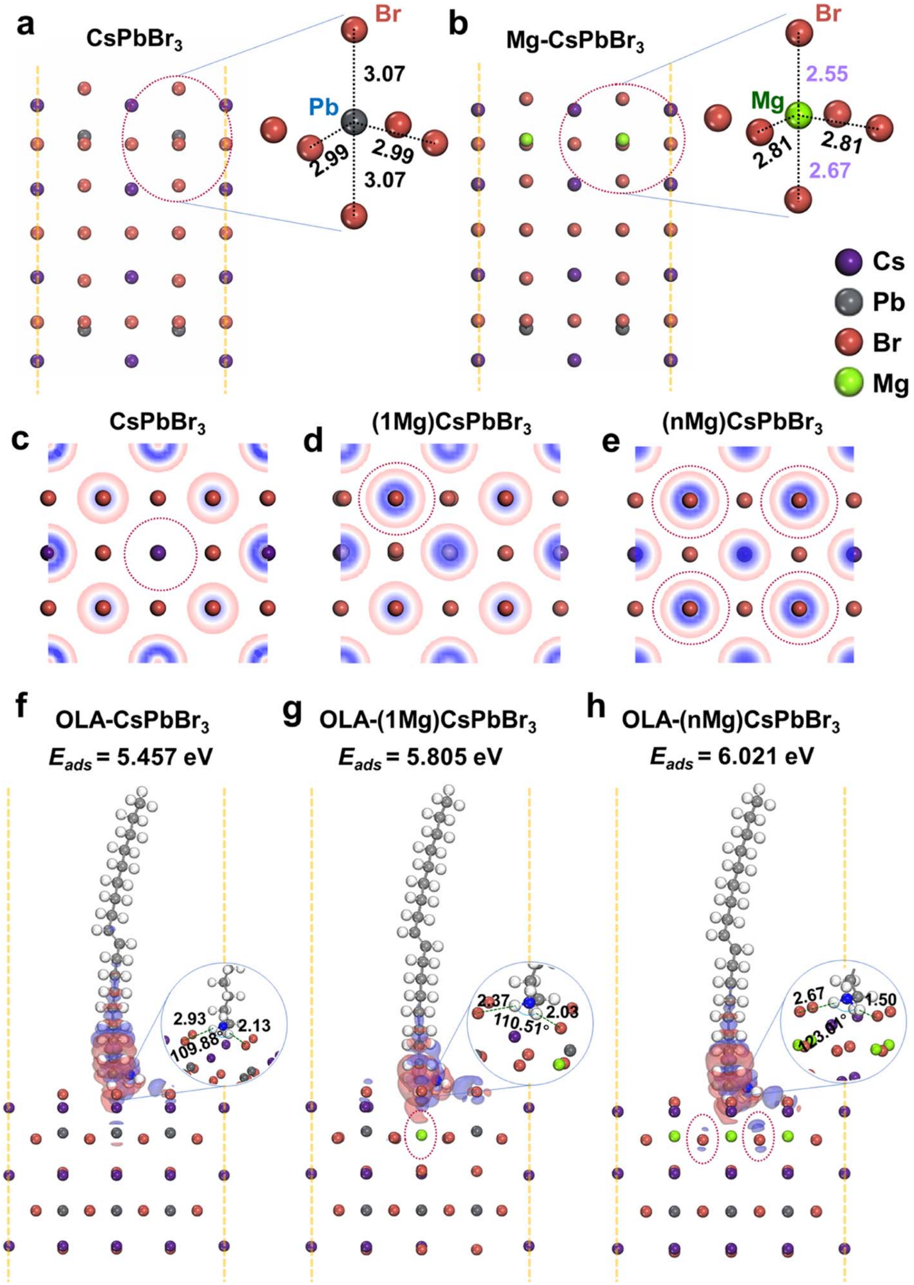

Fig. 2 Surface electronic structure of (a) $CsPbBr_3$, and (b) Mg–$CsPbBr_3$. Insets: the geometries of $[PbBr_6]^{4-}$ and $[MgBr_6]^{4-}$ octahedra with Pb–Br and Mg–Br interatomic distances, respectively. The electron density distribution profiles of (c) $CsPbBr_3$, (d) (1Mg) $CsPbBr_3$, and (e) (*n*Mg) $CsPbBr_3$, respectively, where the blue color indicates an increase in electron density. Differential charge density for (f) OLA-$CsPbBr_3$, (g) OLA-(1Mg)–$CsPbBr_3$, and (h) OLA-(*n*Mg)-$CsPbBr_3$, respectively. Insets: local amplification images of the adsorption configurations. Purple, gray, brown, and green spheres represent Cs, Pb, Br, and Mg atoms, respectively.

b suggest that the LARP-$CsPbBr_3$ NCs possess a similar PL peak and absorption onset in comparison to those of perovskite NCs synthesized through the CSARP process, while the LARP-$CsPbBr_3$ NCs have lower PLQY (*ca.* 70%), revealing their higher trap states. Meanwhile, we further calculate the Urbach energies (E_U) of these samples by plotting the absorption coefficient as a function of photon energy. The value of E_U can be extracted by fitting the exponential part of the Urbach tail according to the following equation:

$$\alpha(E) = \alpha_0 \exp[\sigma(T)(E - E_0)/(k_B T)] \tag{2}$$

where $\alpha(E)$ is the absorption coefficient as a function of photon energy E, E_0 and α_0 are the characteristic parameters of the material, $\sigma(T)$ is the steepness factor, k_B is the Boltzmann constant, T is the absolute temperature, and E_U is defined as $E_U = k_B T/\sigma(T)$. A large value of E_U strongly indicates that the sample suffers from a cumulative effect of impurities, inherent structural disorders, and electron–phonon interaction in the

Open Access Article. Published on 27 July 2023. Downloaded on 7/14/2025 8:56:35 PM.
This article is licensed under a Creative Commons Attribution-NonCommercial 3.0 Unported Licence.

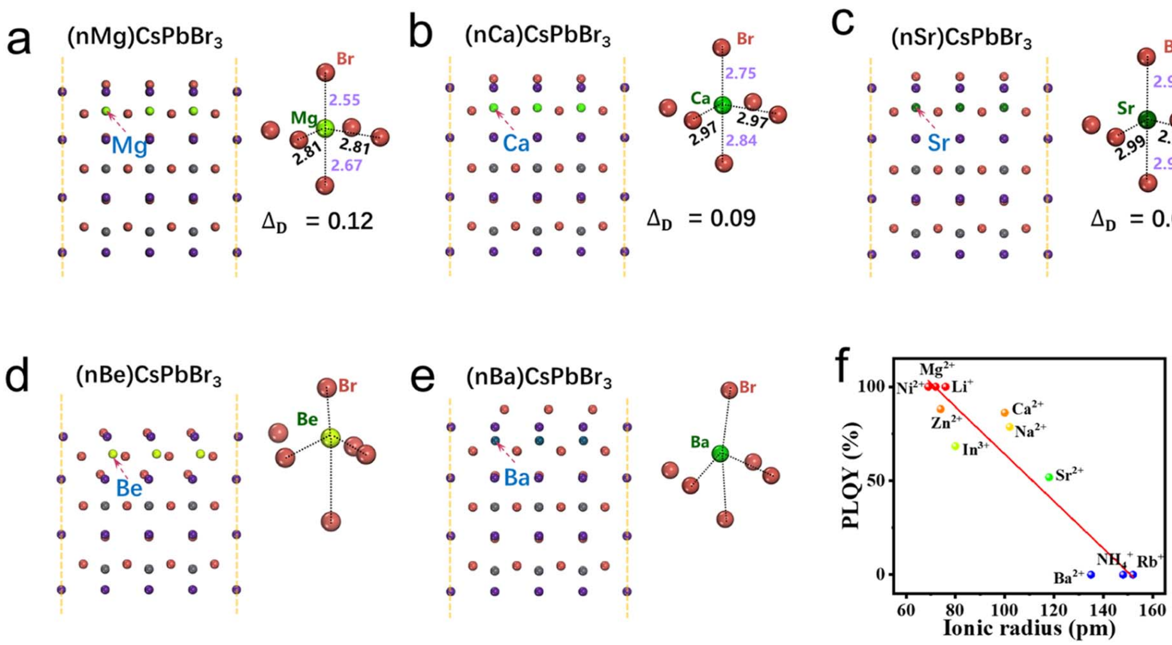

Fig. 3 (a)–(e) Surface polarization of $CsPbBr_3$ NCs based on alkaline-earth metal ions. (f) PLQY *vs.* ionic radius of various metal bromide precursors.

absorption process.[21,47] Fig. 4c shows the fitting curves of LARP- (black lines) and CSARP-$CsPbBr_3$ NCs (green lines). The calculated E_U of the CSARP-$CsPbBr_3$ NCs is 18.1 meV, which is much lower than that of LARP-$CsPbBr_3$ NCs (25.7 meV). These results clearly indicate that $CsPbBr_3$ NCs synthesized *via* the CSARP strategy have a much lower defect density than LARP-$CsPbBr_3$ NCs. This is further supported by the results obtained from the PL decay measurements, as shown in Fig. 4d. The PL decay

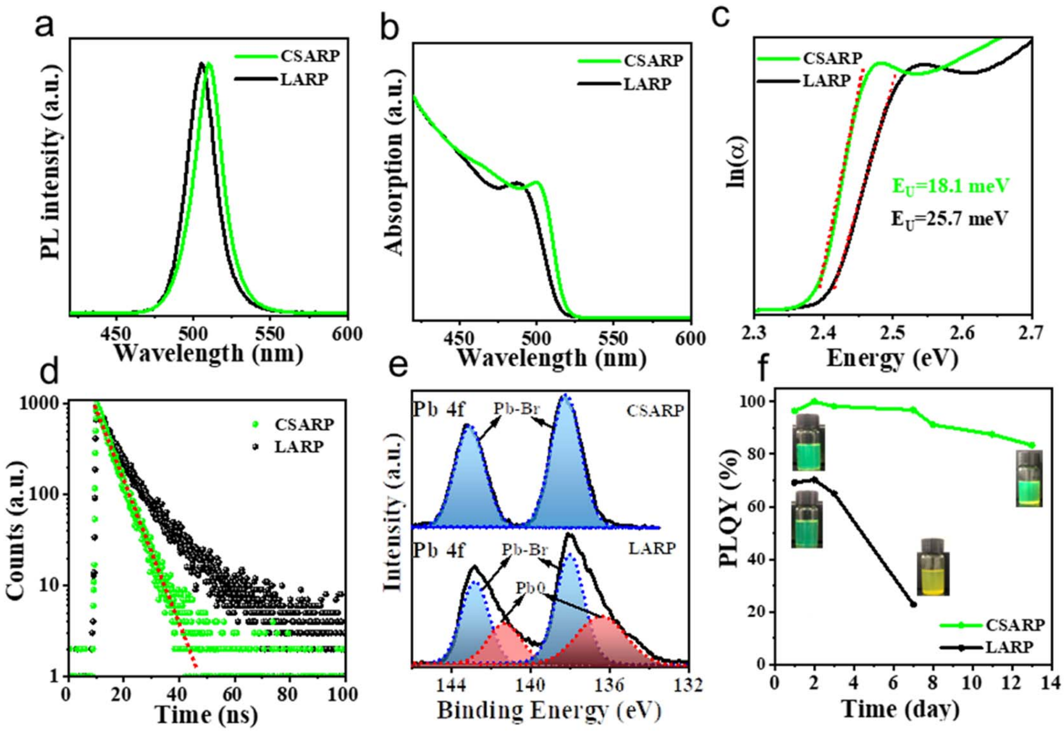

Fig. 4 PL spectra (a), UV-vis absorption spectra (b), Urbach energies (E_U) (c), time-resolved PL spectra (d), XPS spectra (e), and PL stability (f) of CSARP-$CsPbBr_3$ (green lines) and LARP-$CsPbBr_3$ (black lines).

© 2023 The Author(s). Published by the Royal Society of Chemistry

Open Access Article. Published on 27 July 2023. Downloaded on 7/14/2025 8:56:35 PM.
This article is licensed under a Creative Commons Attribution-NonCommercial 3.0 Unported Licence.

kinetics of the CSARP-$CsPbBr_3$ NCs can be well fitted by using the single exponential component. The result of either exciton decay or of carrier trapping at defect sites can be reflected in the PL decay curves. The single exponential component, as well as high PLQY are the fingerprints of pure excitonic decay with minimal nonradiative losses.[48]

Furthermore, X-ray photoelectron spectroscopy (XPS) measurement is performed to monitor the chemical state of the CSARP- and LARP-$CsPbBr_3$ NCs (Fig. 4e and S4†). The high-resolution XPS (HR-XPS) spectra of Pb illustrate distinct differences between these two samples, as shown in Fig. 4e. Two sets of peaks are observed for the LARP-$CsPbBr_3$ NCs. One set of peaks at 138.0 ($4f_{7/2}$) and 142.8 eV ($4f_{5/2}$) are assigned to the internal Pb–Br bond, and another set of shoulder peaks at lower binding energies of 137.5 ($4f_{7/2}$) and 142.4 eV ($4f_{5/2}$) correspond to the Pb^0 species on the surface with Br vacancies.[49] In contrast, only a single set of peaks located at 138.3 ($4f_{7/2}$) and 143.2 eV ($4f_{5/2}$), which are assigned to the internal Pb–Br bond, can be observed for the CSARP-$CsPbBr_3$ NCs. That is to say, the CSARP-$CsPbBr_3$ NCs should have a more ideal structure with lower defect density than the LARP-$CsPbBr_3$ NCs. The long-term stabilities of these samples are further investigated by monitoring the change in their PLQYs with time, as shown in Fig. 4f. One can easily find that the PLQY of the CSARP-$CsPbBr_3$ NCs can be maintained over 90% for 14 days, while the PLQY of LARP-$CsPbBr_3$ NCs shows a drastic decline, and only remains 23% after 7 days. These results clearly confirm the advantage of our synthesis strategy over the LARP process, which can obtain NCs with perfect optical properties, reduced surface defects, and improved stability.

Besides the use of toxic polar solvents with high boiling points, the inability to synthesize pure iodine-based perovskite

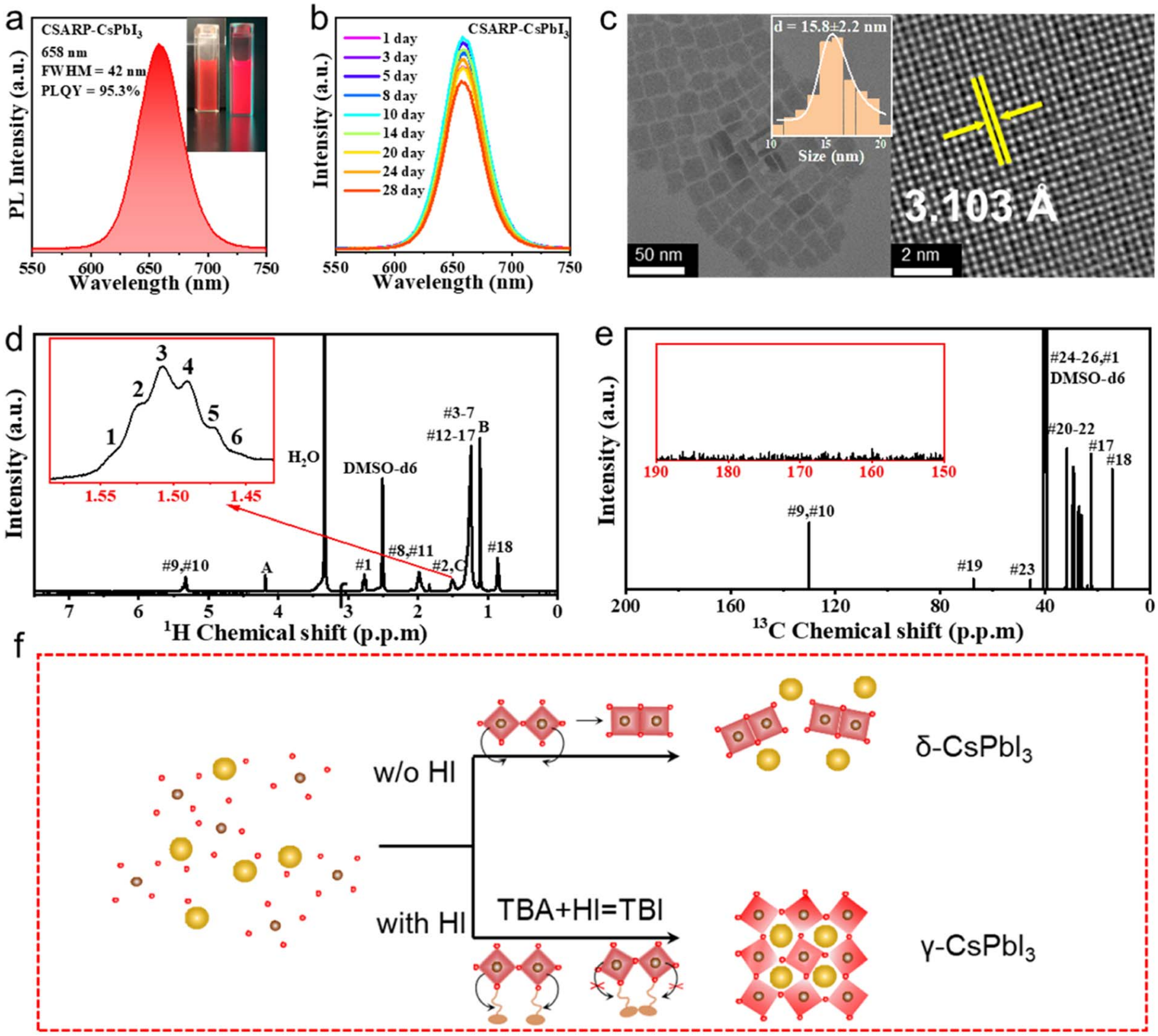

Fig. 5 (a) PL spectra of CSARP-$CsPbI_3$. The insets show photographs under room light (left) and a UV lamp (right, $\lambda = 365$ nm). (b) PL spectra of CSARP-$CsPbI_3$ kept under ambient conditions for different times. (c) TEM and HRTEM images of the CSARP-$CsPbI_3$ NCs. ^1H NMR (d) and ^{13}C NMR (e) spectra (dispersed in DMSO-d_6, at 298 K, with 400 MHz) of CSARP-$CsPbI_3$ NCs. (f) Mechanism diagram of $CSPbI_3$ synthesis by the CSARP strategy at room temperature.

Open Access Article. Published on 27 July 2023. Downloaded on 7/14/2025 8:56:35 PM.
This article is licensed under a Creative Commons Attribution-NonCommercial 3.0 Unported Licence.

NCs is another drawback of the LARP strategy. In comparison, we successfully realize the synthesis of pure $CsPbI_3$ with a high PLQY of 95.3% through the CSARP technique. Impressively, obvious PL can be also observed under room light, as shown in Fig. 5a. In addition, the as-synthesized $CsPbI_3$ NCs have uniform size distribution and good crystallization, as shown in Fig. 5c. Stability tracking results show that the PL spectra of the as-prepared $CsPbI_3$ NCs can maintain 90% of their initial intensity after 28 days of being kept under ambient conditions (Fig. 5b), which is even better than the stability of previously reported $CsPbI_3$ NCs synthesized by the hot-injection process.[22,50] It should be noted here that MgI_2 dissolved in HI rather than water is selected as the iodine precursor for the synthesis of $CsPbI_3$ NCs, as the latter resulted in the formation of the non-luminescent yellow phase (γ-$CsPbI_3$). It is well known that a unimolecular nucleophilic substitution (SN_1) chemical reaction can take place between alcohol and halogenated acid,[51] leading to the formation of halohydrocarbon. Therefore, it is hypothesized that the *in situ* formed *tert*-butyl iodide (TBI) obtained from eqn (3) should be crucial for the successful synthesis of black phase $CsPbI_3$ NCs (Fig. S5†).[52]

$$\text{TBA} + \text{HI} \rightarrow \text{TBI} + H_2O \tag{3}$$

A series of experiments are carried out to verify this supposition, as shown in Fig. S6 and Video S1–4.† It is clearly seen that the use of a MgI_2–HI mixture results in the formation of a black phase, while the yellow phase which arises for the MgI_2–H_2O one at the beginning, is subsequently turned into a mixture of black and yellow phases, and completely transforms into the yellow phase finally. In contrast, when TBI is pre-injected into the solution (containing hexane, TBA, OLA, and OA), the NCs based on the MgI_2–H_2O precursor can maintain the black phase. That is to say, TBI plays a significant role in the formation of the black phase. The change in color for the MgI_2–H_2O one without pre-injected TBI should be ascribed to the formation of a trace amount of TBI induced by the hydrolysis of MgI_2. Furthermore, when MgI_2–H_2O is injected into the solution without TBA (containing hexane, OLA, and OA), the yellow phase emerges for the entire duration of the reaction. In addition, nuclear magnetic resonance (NMR) measurement is performed to further confirm the type of organic ligands adhered on the surface of the as-synthesized $CsPbI_3$ NCs. The characteristic resonance peak of TBI can be observed at 1.50 ppm from the ^1H NMR spectrum shown in Fig. 5d (Fig. S7†). Moreover, this can be further verified by the ^{13}C NMR spectrum (Fig. 5e), where the resonance peaks at 40.0 and 45.6 ppm can be assigned to TBI. Based on these results, it is reasonable to conclude that the formation of black phase $CsPbI_3$ NCs *via* the CSARP technique is dominated by the *in situ* formed TBI, which can also passivate the surface and enhance the stability of the as-synthesized $CsPbI_3$ NCs (Fig. 5f).

Similarly, a series of $CsPbX_3$ NCs with various optical properties are achieved by adjusting their composition (ratio of halides in the mixed halide NCs), as shown in Fig. 6a and Table

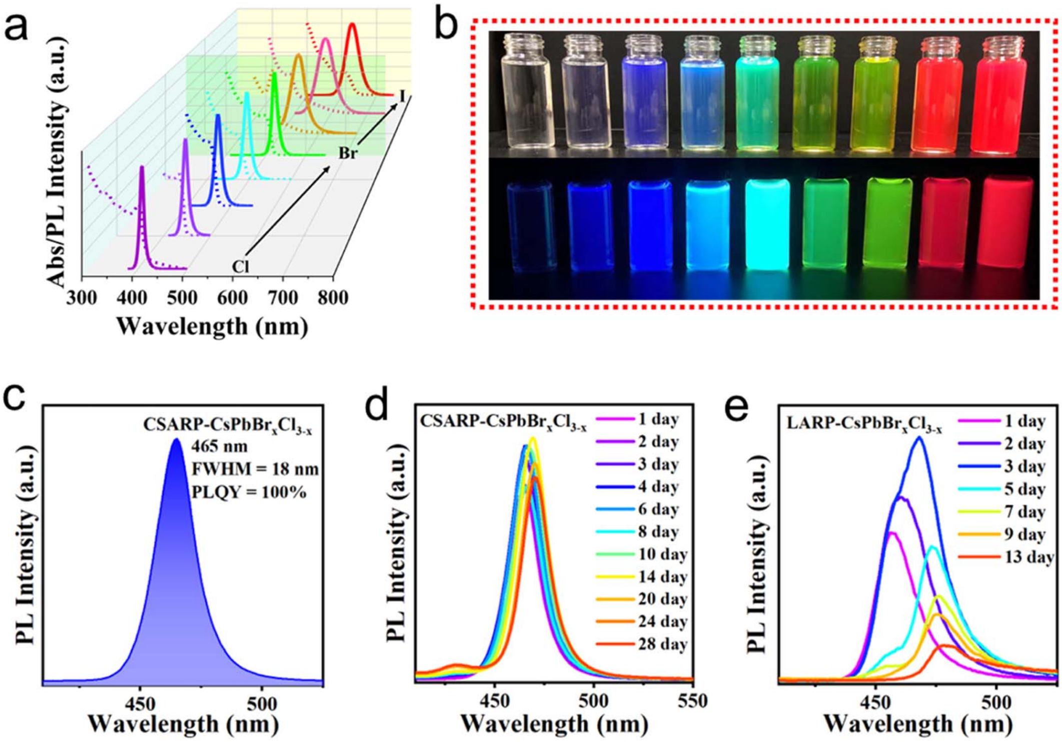

Fig. 6 (a) PL spectra of CSARP-$CsPbX_3$ NCs. (b) Photograph of $CsPbX_3$ NCs with different emission colors under room light (top) and a UV lamp (bottom, $\lambda = 365$ nm). (c) PL spectra of CSARP-$CsPbBr_xCl_{3-x}$. Insets: photographs under room light (left) and a UV lamp (right, $\lambda = 365$ nm). PL spectra of CSARP-$CsPbBr_xCl_{3-x}$ (d) and LARP-$CsPbBr_xCl_{3-x}$ (e) NCs kept under ambient conditions for different times.

© 2023 The Author(s). Published by the Royal Society of Chemistry

Open Access Article. Published on 27 July 2023. Downloaded on 7/14/2025 8:56:35 PM. This article is licensed under a Creative Commons Attribution-NonCommercial 3.0 Unported Licence.

S1.† Distinct PL emission with various colors of these NCs can be see under a UV lamp and room light (Fig. 6b), revealing their outstanding optical properties. $CsPbBr_xCl_{3-x}$ NCs with blue emission is believed to have great potential in blue LEDs; however, the low stability induced by phase segregation is one of the biggest restrictions. Here, we successfully realized the synthesis of $CsPbBr_xCl_{3-x}$ NCs with near unity PLQY in the blue region (465 nm) (Fig. 6c). More importantly, the optical properties of CSARP-$CsPbBr_xCl_{3-x}$ NCs can be well maintained even after 28 days under ambient conditions, as shown in Fig. 6d. For comparison, serious phase segregation and PL decline are observed for the LARP-$CsPbBr_xCl_{3-x}$ NCs (Fig. 6e). That is to say, the CSARP-$CsPbBr_xCl_{3-x}$ NCs exhibit a much slower phase segregation rate and improved stability than LARP-$CsPbBr_xCl_{3-x}$ NCs, which should be attributed to the reduced surface defect density and suppressed ion migration.

Conclusion

In summary, this work provides a simple and environment-friendly strategy to synthesize $CsPbX_3$ NCs with near ideal optical properties and enhanced stabilities. It is found that polarization effects induced by metal ions with small radii significantly enhance the adsorption energy of ligands, which eventually inhibits the formation of surface defects and results in $CsPbX_3$ NCs with near-unity PLQY. Interestingly, the synthesis of black phase $CsPbI_3$ NCs is successfully realized *via* the CSARP approach, which is a serious limitation of the traditional LARP process. Further studies reveal that the *in situ* formed TBI dominates the formation of black phase $CsPbI_3$ NCs, which can also passivate the surface and enhance the stability of $CsPbI_3$ NCs. Moreover, the CSARP strategy can also suppress the ion migration of mixed halide $CsPbX_3$ NCs, which further leads to inhibited phase segregation and enhanced stability.

Experimental section

Chemicals

Lead acetate trihydrate ($PbAc_2 \cdot 3H_2O$, 99.99%), cesium acetate (CsAc, 99.9%), lead chloride ($PbCl_2$, 99.99%), lead bromide ($PbBr_2$, 99.999%), magnesium chloride ($MgCl_2$, 99.9%), magnesium bromide ($MgBr_2$, 99.99%), magnesium iodide (MgI_2, 98%), zinc bromide ($ZnBr_2$, 99.9%), sodium bromide (NaBr, 99.99%), ammonium bromide (NH_4Br, 99.99%), lithium bromide (LiBr, 99.9%), rubidium bromide (RbBr, 99.5%), nickel bromide ($NiBr_2$, 98%), calcium bromide ($CaBr_2$, 98%), strontium bromide ($SrBr_2$, 99%), barium bromide ($BaBr_2$, 99%), indium bromide ($InBr_3$, 99%), hydrobromic acid (HBr, 48%, ACS), hydriodic acid (HI, 45–50%), oleylamine ($C_{18}H_{37}N$, OLA, 80–90%), oleic acid ($C_{18}H_{34}O_2$, OA, AR), *tert*-butanol alcohol ($C_4H_{10}O$, TBA, AR), *n*-hexane (C_6H_{14}, HEX, AR), acetic acid ($C_2H_4O_2$, HAc, AR), isopropyl alcohol (C_3H_8O, IPA, AR), methyl acetate ($C_3H_6O_2$, MeOAc, AR), ethyl acetate ($C_4H_8O_2$, EA, AR), *N*,*N*-dimethylformamide (C_3H_7NO, DMF, AR), 1-octadecene ($C_{18}H_{36}$, ODE, >90%), dimethyl sulfoxide-d$_6$ (C_2D_6SO, DMSO-d$_6$, 99.9%), and *tert*-butyl iodide (C_4H_9I, TBI, > 95.0%) were purchased from Aladdin Industrial Corporation, China. Toluene (C_7H_8, AR) was purchased from Sinopharm Chemical Reagent Co., Ltd. All of the reagents were commercial and used without further purification. Deionized water was used in all experiments.

Preparations of precursor solutions

Precursor 1. 1 mmol CsAc and 1 mmol $PbAc_2$ were dissolved in 2 mL HAc at room temperature under ambient conditions.

Precursor 2. MgX_2 ($X = Cl$, Br, the total amount was kept at 2 mmol) was dissolved in H_2O (1 mL) at room temperature under ambient conditions.

Precursor 3. MgX_2 ($X = Br$, I, the total amount was kept at 2 mmol) was dissolved in HX (1 mL) ($X = Br$, I) at room temperature under ambient conditions.

Synthesis of CSARP-$CsPbX_3$ NCs

HEX and TBA were mixed as reaction solvent, 200 μL OA and 200 μL OLA were used as ligands and added into the above mixture under intense stirring to form a homogeneous solution. Then, 50 μL Precursor 1 was injected and stirred evenly for 5 min. After that, 50 μL Precursor 2 (Precursor 3 was used for iodide-contained reactions) was added and stirred continuously for 30–120 min to obtain desired $CsPbX_3$ NCs. All the reactions were carried out at room temperature under ambient conditions. The volume ratio of HEX to TBA is important for this strategy, which was tuned from 1 : 4 to 4 : 1. The detailed volume used for various NCs can be found in Table S2.† The crude solution was centrifuged at 16 000 rpm for 10 min, and the precipitate was dispersed in 5 mL hexane after discarding the supernatant. Whereafter, another centrifugation process was carried out (8000 rpm for 5 min) to remove oversized NCs. Finally, the supernatant containing $CsPbX_3$ NCs was saved.

Synthesis of CSARP-$CsPbBr_3$ NCs using various kinds of metal bromide precursors

All the steps were the same as in the above process except usage of various metal bromides for the preparation of Precursor 2.

Synthesis of LARP-$CsPbX_3$ NCs

0.4 mmol PbX_2 and 0.4 mmol CsX were dissolved in 10 mL DMF, 1 mL OA and 0.5 mL OLA were added to stabilize this precursor solution. Then, 1 mL of the precursor solution was quickly added to 10 mL toluene under vigorous stirring to obtain $CsPbX_3$ NCs.

Characterization

Powder XRD patterns were recorded using a Bruker D8 Advance X-ray diffractometer (Cu Kα, $\lambda = 1.5406$ Å). TEM analysis was carried out with an FEI Talos F200X microscope at an operating voltage of 200 kV. UV-vis absorption spectra were obtained using a Specord 200 Plus spectrophotometer. PL, PLQYs, and PL lifetimes were obtained by using an EI-FLS1000 fluorescence spectrometer (Edinburgh Instruments) equipped with an integrating sphere. XPS measurements were performed using an

Open Access Article. Published on 27 July 2023. Downloaded on 7/14/2025 8:56:35 PM.
This article is licensed under a Creative Commons Attribution-NonCommercial 3.0 Unported Licence.

ESCALAB Xi+ (Thermo Fischer), monoatomic Ar^+ ions were employed for XPS etching with various depths (the etching rate was estimated through Ta_2O_5, the data were collected at each 2 nm depth); all the XPS data are calibrated by using the C 1s core level. A Bruker AVANCE III (400 MHz) was used to record the NMR data.

Computational methods

Electronic structure calculations were performed systematically within the framework of the density functional theory (DFT) formalism as implemented in Materials Studio (MS) to explore the electronic properties of pure $CsPbBr_3$, 1Mg-, and *n*Mg-$CsPbBr_3$. General gradient approximation (GGA) in the form of a Perdew–Burke–Ernzerhof (PBE) exchange-correlation functional was employed for optimizing the geometrical structure. Each (001) $CsPbBr_3$ slab consisted of 7 single layers, and a large vacuum spacing of >20 Å was used to prevent inter-slab interactions. Ligands and the top four layers of the $CsPbBr_3$ slab were fully relaxed until the structure satisfied the following relaxation criteria: the energy cutoff used throughout the calculations was set at 700 eV, while the first Brillouin zone integrations were sampled using a 7 × 7 × 1 Monkhorst pack for the ionic relaxation of the system. The convergence thresholds were set at 0.002 Hartree per Å for the maximum force, 0.005 Å for the maximum displacement, and 1.0×10^{-5} Hartree for the energy change.

Data availability

The data supporting this study are available within the main text and the ESI.†

Author contributions

K. C. and Z. G. conceived the study; K. C., Z. G., Y. L., and G. L. designed the experiments and supervised the research. K. C., Z. G., and Z. W. performed the experiments and analyzed the data; M. G., X. T., W. X., X. J., and W. L. helped with the data collection; K. C., Z. G., Y. L., and G. L. wrote and revised the manuscript; all authors discussed the results and approved the final version of the manuscript.

Conflicts of interest

There are no conflicts to declare.

Acknowledgements

This work was supported by the National Natural Science Foundation of China (NSFC No. 52072349 and 12174298), the Natural Science Foundation of Zhejiang Province (No. LZ22A040005 and LR22E020004), the Natural Science Foundation of Hubei Province (No. 2022CFB654), the Guangdong Basic and Applied Basic Research Foundation (No. 2023A1515030021), the Shenzhen Science and Technology Program (No. JCYJ20220530162405012 and JCYJ20210324135002007), the Hainan Provincial Joint Project of Sanya Yazhou Bay Science and Technology City (No. 520LH053), the 111 Project (No. B18038), the Fundamental Research Funds for the Central Universities (No. 2021Szvup104), the State Key Laboratory of Advanced Technology for Materials Synthesis and Processing (Wuhan University of Technology) (No. 2022-KF-30), and the State Key Laboratory of Silicate Materials for Architectures (Wuhan University of Technology) (No. SYSJJ2022-11).

References

1 A. Kojima, K. Teshima, Y. Shirai and T. Miyasaka, *J. Am. Chem. Soc.*, 2009, **131**, 6050–6051.

2 L. Protesescu, S. Yakunin, M. I. Bodnarchuk, F. Krieg, R. Caputo, C. H. Hendon, R. X. Yang, A. Walsh and M. V. Kovalenko, *Nano Lett.*, 2015, **15**, 3692–3696.

3 A. Swarnkar, A. R. Marshall, E. M. Sanehira, B. D. Chernomordik, D. T. Moore, J. A. Christians, T. Chakrabarti and J. M. Luther, *Science*, 2016, **354**, 92–95.

4 Y. Dong, Y.-K. Wang, F. Yuan, A. Johnston, Y. Liu, D. Ma, M.-J. Choi, B. Chen, M. Chekini, S.-W. Baek, L. K. Sagar, J. Fan, Y. Hou, M. Wu, S. Lee, B. Sun, S. Hoogland, R. Quintero-Bermudez, H. Ebe, P. Todorovic, F. Dinic, P. Li, H. T. Kung, M. I. Saidaminov, E. Kumacheva, E. Spiecker, L.-S. Liao, O. Voznyy, Z.-H. Lu and E. H. Sargent, *Nat. Nanotechnol.*, 2020, **15**, 668–674.

5 K. Chen, W. Jin, Y. Zhang, T. Yang, P. Reiss, Q. Zhong, U. Bach, Q. Li, Y. Wang, H. Zhang, Q. Bao and Y. Liu, *J. Am. Chem. Soc.*, 2020, **142**, 3775–3783.

6 K. Chen, Y. Wang, J. Liu, J. Kang, Y. Ge, W. Huang, Z. Lin, Z. Guo, Y. Zhang and H. Zhang, *Nanoscale*, 2019, **11**, 16852–16859.

7 J. S. Yao, J. Ge, K. H. Wang, G. Zhang, B. S. Zhu, C. Chen, Q. Zhang, Y. Luo, S. H. Yu and H. B. Yao, *J. Am. Chem. Soc.*, 2019, **141**, 2069–2079.

8 C.-T. Wang, K. Chen, P. Xu, F. Yeung, H.-S. Kwok and G. Li, *Adv. Funct. Mater.*, 2019, **29**, 1903155.

9 Q. Zeng, X. Zhang, Q. Bing, Y. Xiong, F. Yang, H. Liu, J.-y. Liu, H. Zhang, W. Zheng, A. L. Rogach and B. Yang, *ACS Energy Lett.*, 2022, **7**, 1963–1970.

10 J. Ye, Z. Li, D. J. Kubicki, Y. Zhang, L. Dai, C. Otero-Martinez, M. A. Reus, R. Arul, K. R. Dudipala, Z. Andaji-Garmaroudi, Y. T. Huang, Z. Li, Z. Chen, P. Muller-Buschbaum, H. L. Yip, S. D. Stranks, C. P. Grey, J. J. Baumberg, N. C. Greenham, L. Polavarapu, A. Rao and R. L. Z. Hoye, *J. Am. Chem. Soc.*, 2022, **144**, 12102–12115.

11 Z. L. Tseng, L. C. Chen, L. W. Chao, M. J. Tsai, D. Luo, N. R. Al Amin, S. W. Liu and K. T. Wong, *Adv. Mater.*, 2022, **34**, 2109785.

12 D. Luo, X. Li, A. Dumont, H. Yu and Z. H. Lu, *Adv. Mater.*, 2021, **33**, e2006004.

13 J. De Roo, M. Ibáñez, P. Geiregat, G. Nedelcu, W. Walravens, J. Maes, J. C. Martins, I. Van Driessche, M. V. Kovalenko and Z. Hens, *ACS Nano*, 2016, **10**, 2071–2081.

14 K. Chen, C. Wang, Z. Peng, K. Qi, Z. Guo, Y. Zhang and H. Zhang, *Coord. Chem. Rev.*, 2020, **418**, 213333.

15 J. Shamsi, A. S. Urban, M. Imran, L. De Trizio and L. Manna, *Chem. Rev.*, 2019, **119**, 3296–3348.

© 2023 The Author(s). Published by the Royal Society of Chemistry

Open Access Article. Published on 27 July 2023. Downloaded on 7/14/2025 8:56:35 PM.
This article is licensed under a Creative Commons Attribution-NonCommercial 3.0 Unported Licence.

16 Q. Zhao, R. Han, A. R. Marshall, S. Wang, B. M. Wieliczka, J. Ni, J. Zhang, J. Yuan, J. M. Luther, A. Hazarika and G. R. Li, *Adv. Mater.*, 2022, **34**, e2107888.

17 L. Liu, A. Najar, K. Wang, M. Du and S. F. Liu, *Adv. Sci.*, 2022, **9**, 2104577.

18 Y. Wang, K. Chen, H. Hao, G. Yu, B. Zeng, H. Wang, F. Zhang, L. Wu, J. Li, S. Xiao, J. He, Y. Zhang and H. Zhang, *Nanoscale*, 2019, **11**, 2637–2643.

19 Y. Wang, J. Yuan, X. Zhang, X. Ling, B. W. Larson, Q. Zhao, Y. Yang, Y. Shi, J. M. Luther and W. Ma, *Adv. Mater.*, 2020, **32**, 2000449.

20 H. Wang, F. Ye, J. Sun, Z. Wang, C. Zhang, J. Qian, X. Zhang, W. C. H. Choy, X. W. Sun, K. Wang and W. Zhao, *ACS Energy Lett.*, 2022, **7**, 1137–1145.

21 F. Liu, Y. Zhang, C. Ding, S. Kobayashi, T. Izuishi, N. Nakazawa, T. Toyoda, T. Ohta, S. Hayase, T. Minemoto, K. Yoshino, S. Dai and Q. Shen, *ACS Nano*, 2017, **11**, 10373–10383.

22 J. Pan, Y. Shang, J. Yin, M. De Bastiani, W. Peng, I. Dursun, L. Sinatra, A. M. El-Zohry, M. N. Hedhili, A.-H. Emwas, O. F. Mohammed, Z. Ning and O. M. Bakr, *J. Am. Chem. Soc.*, 2018, **140**, 562–565.

23 Y. Hassan, J. H. Park, M. L. Crawford, A. Sadhanala, J. Lee, J. C. Sadighian, E. Mosconi, R. Shivanna, E. Radicchi, M. Jeong, C. Yang, H. Choi, S. H. Park, M. H. Song, F. De Angelis, C. Y. Wong, R. H. Friend, B. R. Lee and H. J. Snaith, *Nature*, 2021, **591**, 72–77.

24 H. Zhu, Y. Pan, C. Peng, H. Lian and J. Lin, *Angew. Chem., Int. Ed.*, 2022, **61**, e202116702.

25 Q. A. Akkerman, T. P. T. Nguyen, S. C. Boehme, F. Montanarella, D. N. Dirin, P. Wechsler, F. Beiglböck, G. Rainò, R. Erni, C. Katan, J. Even and M. V. Kovalenko, *Science*, 2022, **377**, 1406–1412.

26 W. Yin, M. Li, W. Dong, X. Zhang and W. Zheng, *Angew. Chem., Int. Ed. Engl.*, 2023, **135**, e202303462.

27 F. Li, X. Zhang, J. Shi, L. Jin, J. Qiao, J. Guo, H. Yin, Y. Li, J. Yuan and W. Ma, *Adv. Funct. Mater.*, 2023, DOI: **10.1002/adfm.202302542**.

28 J. N. Yang, Z. Y. Ma, J. D. Luo, J. J. Wang, C. Ye, Y. Zhou, Y. C. Yin, X. C. Ru, T. Chen, L. Y. Li, L. Z. Feng, K. H. Song, J. Ge, Q. Zhang and H. B. Yao, *Nano Lett.*, 2023, **23**, 3385–3393.

29 H. Zhu, G. Tong, J. Li, E. Xu, X. Tao, Y. Sheng, J. Tang and Y. Jiang, *Adv. Mater.*, 2022, **34**, 2205092.

30 W. Sun, R. Yun, Y. Liu, X. Zhang, M. Yuan, L. Zhang and X. Li, *Small*, 2023, **19**, e2205950.

31 N. Fiuza-Maneiro, K. Sun, I. López-Fernández, S. Gómez-Graña, P. Müller-Buschbaum and L. Polavarapu, *ACS Energy Lett.*, 2023, **8**, 1152–1191.

32 L. De Trizio, I. Infante and L. Manna, *Acc. Chem. Res.*, 2023, **56**, 1815–1825.

33 K. Chen, Q. Zhong, W. Chen, B. Sang, Y. Wang, T. Yang, Y. Liu, Y. Zhang and H. Zhang, *Adv. Funct. Mater.*, 2019, **29**, 1900991.

34 J. Wang, J. Li, Y. Zhou, C. Yu, Y. Hua, Y. Yu, R. Li, X. Lin, R. Chen, H. Wu, H. Xia and H. L. Wang, *J. Am. Chem. Soc.*, 2021, **143**, 7759–7768.

35 M. Zhang, Q. Chen, R. Xue, Y. Zhan, C. Wang, J. Lai, J. Yang, H. Lin, J. Yao, Y. Li, L. Chen and Y. Li, *Nat. Commun.*, 2019, **10**, 4593.

36 H. Liu, Z. Lu, W. Zhang, J. Wang, Z. Lu, Q. Dai, X. Qi, Y. Shi, Y. Hua, R. Chen, T. Shi, H. Xia and H. L. Wang, *Adv. Sci.*, 2022, **9**, 2203640.

37 T. Yang, W. Zhao, X. Liu and S. Liu, *Adv. Energy Mater.*, 2023, **13**, 2204192.

38 J. Zhang, B. Che, W. Zhao, Y. Fang, R. Han, Y. Yang, J. Liu, T. Yang, T. Chen, N. Yuan, J. Ding and S. Liu, *Adv. Mater.*, 2022, **34**, 2202735.

39 B. Guo, R. Lai, S. Jiang, L. Zhou, Z. Ren, Y. Lian, P. Li, X. Cao, S. Xing, Y. Wang, W. Li, C. Zou, M. Chen, Z. Hong, C. Li, B. Zhao and D. Di, *Nat. Photonics*, 2022, **16**, 637–643.

40 G. Li, Z. Su, L. Canil, D. Hughes, M. H. Aldamasy, J. Dagar, S. Trofimov, L. Wang, W. Zuo, J. J. Jerónimo-Rendon, M. M. Byranvand, C. Wang, R. Zhu, Z. Zhang, F. Yang, G. Nasti, B. Naydenov, W. C. Tsoi, Z. Li, X. Gao, Z. Wang, Y. Jia, E. Unger, M. Saliba, M. Li and A. Abate, *Science*, 2023, **379**, 399–403.

41 T. Li, J. Xu, R. Lin, S. Teale, H. Li, Z. Liu, C. Duan, Q. Zhao, K. Xiao, P. Wu, B. Chen, S. Jiang, S. Xiong, H. Luo, S. Wan, L. Li, Q. Bao, Y. Tian, X. Gao, J. Xie, E. H. Sargent and H. Tan, *Nat. Energy*, 2023, **8**, 610–620.

42 Q. Chen, C. Wang, Y. Li and L. Chen, *J. Am. Chem. Soc.*, 2020, **142**, 18281–18292.

43 X. Li, Y. Wu, S. Zhang, B. Cai, Y. Gu, J. Song and H. Zeng, *Adv. Funct. Mater.*, 2016, **26**, 2435–2445.

44 Y. Yang, C. Hou and T. X. Liang, *Phys. Chem. Chem. Phys.*, 2021, **23**, 7145–7152.

45 S. Jeon, M. C. Jung, J. Ahn, H. K. Woo, J. Bang, D. Kim, S. Y. Lee, H. Y. Woo, J. Jeon, M. J. Han, T. Paik and S. J. Oh, *Nanoscale Horiz.*, 2020, **5**, 960–970.

46 J.-K. Chen, J.-P. Ma, S.-Q. Guo, Y.-M. Chen, Q. Zhao, B.-B. Zhang, Z.-Y. Li, Y. Zhou, J. Hou, Y. Kuroiwa, C. Moriyoshi, O. M. Bakr, J. Zhang and H.-T. Sun, *Chem. Mater.*, 2019, **31**, 3974–3983.

47 C. Zheng, C. Bi, F. Huang, D. Binks and J. Tian, *ACS Appl. Mater. Interfaces*, 2019, **11**, 25410–25416.

48 W. J. Mir, A. Alamoudi, J. Yin, K. E. Yorov, P. Maity, R. Naphade, B. Shao, J. Wang, M. N. Lintangpradipto, S. Nematulloev, A. H. Emwas, A. Genovese, O. F. Mohammed and O. M. Bakr, *J. Am. Chem. Soc.*, 2022, **144**, 13302–13310.

49 Y. Cai, H. Wang, Y. Li, L. Wang, Y. Lv, X. Yang and R.-J. Xie, *Chem. Mater.*, 2019, **31**, 881–889.

50 Y. Tang, A. Lesage and P. Schall, *J. Mater. Chem. C*, 2020, **8**, 17139–17156.

51 R. Bruckner, *Organic mechanisms*, Springer, 2010.

52 D. Jia, J. Chen, X. Mei, W. Fan, S. Luo, M. Yu, J. Liu and X. Zhang, *Energy Environ. Sci.*, 2021, **14**, 4599–4609.

© 2023 The Author(s). Published by the Royal Society of Chemistry